CodeOceanOnly Results

The figures shown and discussed in this document are generated and reported specifically in this CodeOcean capsule, and not the associated manuscript "An Injectable Meta-biomaterial: From Design and Simulation to In-vivo Shaping and Tissue induction" by A. Béduer et al.[1], nor in its supporting information.

These figures portray technical or highly detailed results which may be of some interest in the analysis and discussion of the data contained in this capsule. They were however not deemed to be of sufficiently general interest to be directly associated with the publication[1].

The CodeOceanOnly figures are produces by the scripts in /code/Data analysis/Figures_Codeocean_only, and are labelled consecutively from C1 to C13. The figures themselves are available in the Results section at /results/Figures_Codeocean_only, along with detailed textual output where applicable.

The statistical test details associated with these figures and their evaluation are tabulated in "Statistical Reporting.xlsx" (located at /code/Documentation/Statistical Reporting.xlsx in this CodeOcean capsule, hitherto referred to as "Statistical Reporting.xlsx").

1. Additional simulation results

The two figures C1 and C2 shown here relate to details regarding the influence of the model parameter of particle packing density (nominal solid phase volume[2]), on simulated rheological properties. Particularly, the influence of the packing density on the plateau G' value and the yield strain are studied; see Figure 2f of the main manuscript[1] for the definition of these parameters (the plateau G' value is point 3 in Figure 2f, the yield strain is point 4).

1.1. Packing density and low-strain plateau modulus G'

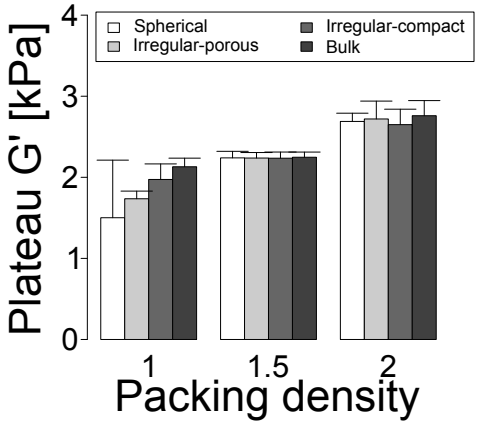

Figure C1. Influence of packing density ϕ on low-strain G' plateau modulus. Other than the particular values indicated in the figure, the common general model parameters were: Young modulus of the constituent material E=10kPa, friction coefficient $\mu = 0.01$, and

removal of a fraction of χ=0.4 of the permanent crosslinks to emulate the porous particles («irregular-porous» in the figure).

Figure C1 shows the quantitative relation between the packing density (expressed as the nominal phase volume[2] ϕ) and the low-strain plateau G' value. For each type of particles (spherical, irregular-compact, irregular-porous as emulated by removal of 40% of the permanent crosslinks, and bulk) there is a highly significant positive relation between packing density and plateau G' value as evaluated at 0.1% strain: $P<4*10^{-4}$ for the spherical case, $P<6*10^{-11}$ for the porous particle case, $P<8*10^{-5}$ for the compact particles, and $P<8*10^{-6}$ for the simulated bulk material, all P-values after Bonferroni correction for 4 tests, "Statistical Reporting.xlsx", item 67).

The dependency observed in the simulations for the emulated porous particles is weaker than our experimental observations indicate (power-law with an exponent of 2.3, see Supporting Information of the publication[1], Figure S10 and Table S5-1). Most likely, this reflects a contact law that is not completely appropriate for the experimental implementation. Indeed, the contact law used here is close to the Hertzian contact law[3] for spherical particles, and the increase of plateau G' by a factor of about 1.8 for packing density increasing from 1 to 2 in Figure C1 is in good agreement with literature data (Figure 4 in [2]).

1.2. Packing density and yield strain

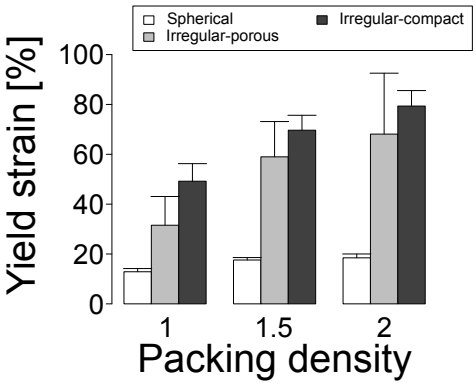

Figure C2. Influence of packing density ϕ on yield strain. Other than the particular values indicated in the figure, the common general model parameters were: Young modulus of the constituent material E=10kPa, friction coefficient $\mu = 0.01$, and removal of a fraction of χ=0.4 of the permanent crosslinks to emulate the porous particles («irregular-porous» in the figure).

In our simulations, packing density also influences yield strain (Figure 2g in the main text[1], Packing / feature 4 in Figure 2f also of the main text[1]). We here investigated how strong this effect could be. Figure C2 shows that there is a substantial effect for each particle type ($P=9.9*10^{-5}$ for the spherical particles, $P=4.8*10^{-3}$ for the porous, and $P=3.8*10^{-5}$ for the compact particles, "Statistical Reporting.xlsx", item 68). Nevertheless, for all practical purposes, packing density cannot be adjusted to sufficient values for a spherical microgel suspension to reach yield strains possible with irregular particles.

2. Pore size and pore fraction analysis: image acquisition and analysis

Pore space characteristics in both the EPI biomaterial and Sephacryl S200 are analyzed in detail in the main manuscript[1] and also chapter 4 of its associated Supporting Information.

Here, details of the image acquisition and analysis to obtain pore fraction and local pore size are detailed for reference.

2.1. Image acquisition

We analyze the geometrical pore space characteristics by confocal imaging on samples with known dry polymer weight concentration. For obtaining sufficient fluorescence from the EPI biomaterial, we stained it by using Rhodamine 6G hydrochloride solution (5 microgram/mL in deionized water), followed by thorough rinsing in deionized water to remove free dye, and readjustment to known dry weight. The Sephacryl S200 reference material is sufficiently autofluorescent by excitation in the UV and emission in the blue to obviate the need for staining.

We acquired images at moderately high resolution (20x) for this analysis, using a Zeiss LSM800 confocal microscope.

2.2. Image treatment

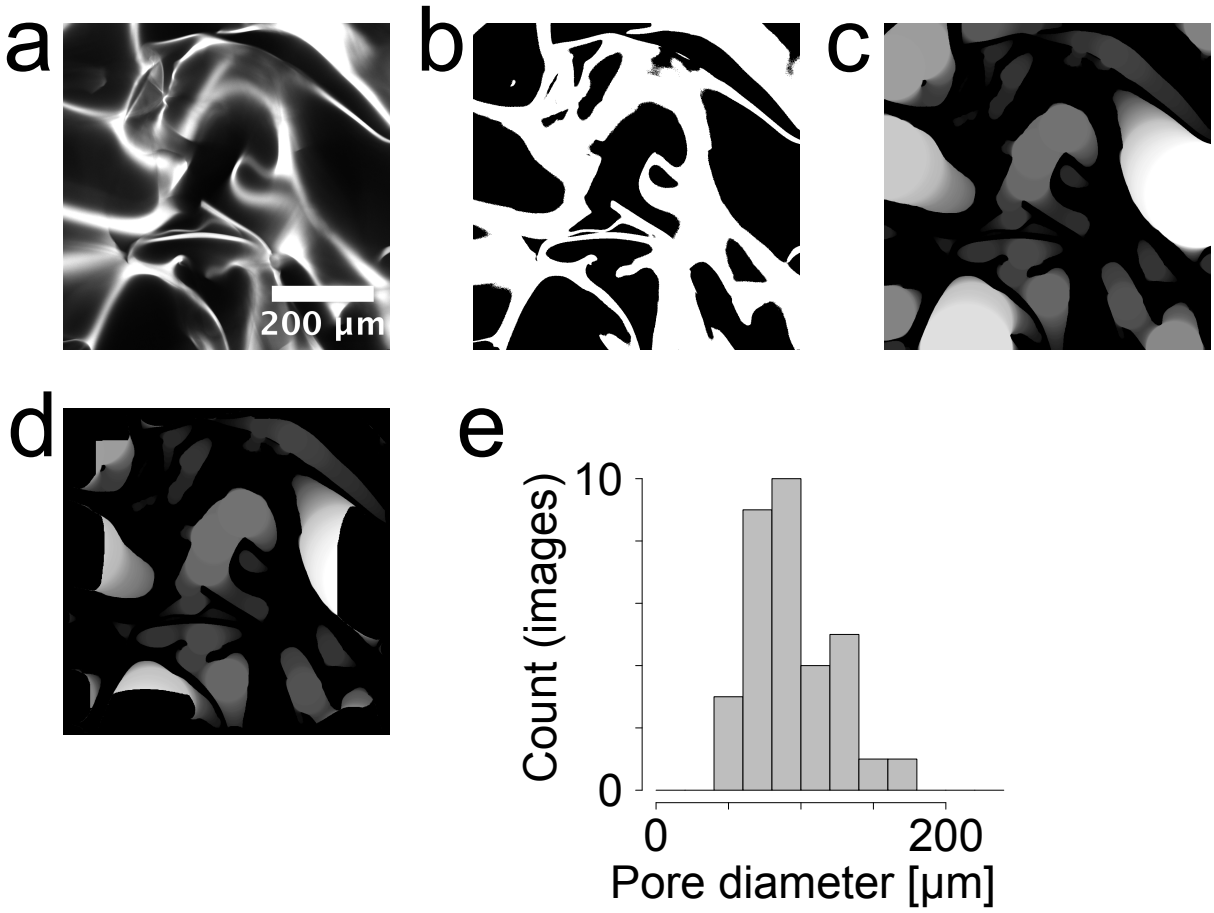

*Figure C3. Pore diameter size determination method. Samples were stained with 5 microgram/mL Rhodamine 6G in deionized water, followed by extensive washing in deionized water and readjustment to the initial dry weight polymer concentration. a) Confocal fluorescence images were then acquired (Zeiss, LSM700, 20x objective). b) Visually, a threshold value was determined allowing to represent the skeleton of the walls enclosing the pores. c) Based on this threshold, the ImageJ pore size determination plugin available in the publicly available xlib plugin collection was run. On 2D images, this plugin fits maximal circles into the pore space, allowing to assign a local pore size to each pixel located in the pore space. The grey scale value shown in Figure C3c corresponds to the local pore radius value. d) To exclude edge effects, pixels where the associated pore circle touches or overlaps the edges were excluded. d) Averaging the remaining pore pixels over the image, one obtains an average pore diameter (by respecting d=2*r, n.b). The histogram shows the distribution of such average pore diameters over the 33 confocal images we acquired for the 27mg/mL EPI biomaterial concentration.*

From confocal imaging, the pore fraction is obtained by manual thresholding to outline the walls (bright) as compared to the pore space (dark). The pore fraction is then estimated by quantifying the number of bright pixels as compared to the total number of pixels.

The pore diameter is evaluated based on the maximal sphere fitting algorithm implemented by Münch et al.[4,5] The algorithm is outlined in Figure C3, taking a confocal image on an EPI biomaterial sample adjusted to 27mg/mL as an example (Figure C3a).

As for the pore fraction, the image is binarized by thresholding in Fiji[6] (Figure C3b). We then use the Fiji plugin by Beat Münch, available at the time of writing at ftp://ftp.empa.ch/pub/empa/outgoing/BeatsRamsch/lib/, // xlib_.jar to fit maximal circles into the pore space. A continuous pore size distribution is obtained by assigning to each pore pixel the radius of the local maximal sphere (Figure C3c). To avoid edge effects due to absence of information of how the pores would continue beyond the image's edges, we remove pore pixels from the statistics that are closer than one local pore radius to an edge (Figure C3d). From the remaining intensities within the pore space, we obtain the mean pore diameter by averaging and multiplication by 2 as the diameter of a circle is twice its radius. Figure C3e shows the man pore sizes thus obtained for the 33 images we acquired for the 27mg/mL dry weight concentration sample of the EPI biomaterial as a histogram.

3. Yield strain from the intersection of elastic modulus G' and viscous modulus G'' curves

The information provided in this section completes chapter 6 of the Supporting Information document associated with the main publication[1].

Indeed, we use the cross-over of G' and G'' curves in oscillatory rheology to define the yield strain. This is because the main method for establishment of yield characteristics involves flow curves[7]. This yields a precise estimation of yield stress, but the very nature of the test (imposed constant deformation rate) makes it difficult to estimate the yield strain. For this reason, we used the crossing point of the G' and G'' in oscillatory rheology. Here, we provide data comparing the established flow curve method to the propose intersection method. As a readout, we use the yield stress, as both methods are able to evaluate this parameter. Reasonable agreement regarding the yield stress between the two methods is regarded as an indication of the validity of the G' / G'' intersection method.

The yield point is the point where an externally applied flow leads to significant flow and permanent deformation[7]. The yield point is typically estimated from linear shear rheometry[7,8]. For this, one acquires flow curves[7], which report the steady-state stress as a function of imposed, constant deformation rate. The plateau stress limit at low deformation (typically on the order of $1s^{-1}$, in all cases $<10s^{-1}$) indicates the yield stress.[7,8]

The crossing of the G' and G'' curves when plotted against strain and stress applied during oscillatory shear rheology is an alternative method to estimate the yield stress and strain value. Indeed, the crossing point between the G' and G'' curves indicates the transition from a predominantly solid to a predominantly liquid behavior[8], and should thus yield an estimation of the yield point, both regarding stress and strain. Here, we compare yield stress evaluation by the flow curve method versus the G'/G'' crossing method to validate the use of the G' / G'' crossing method.

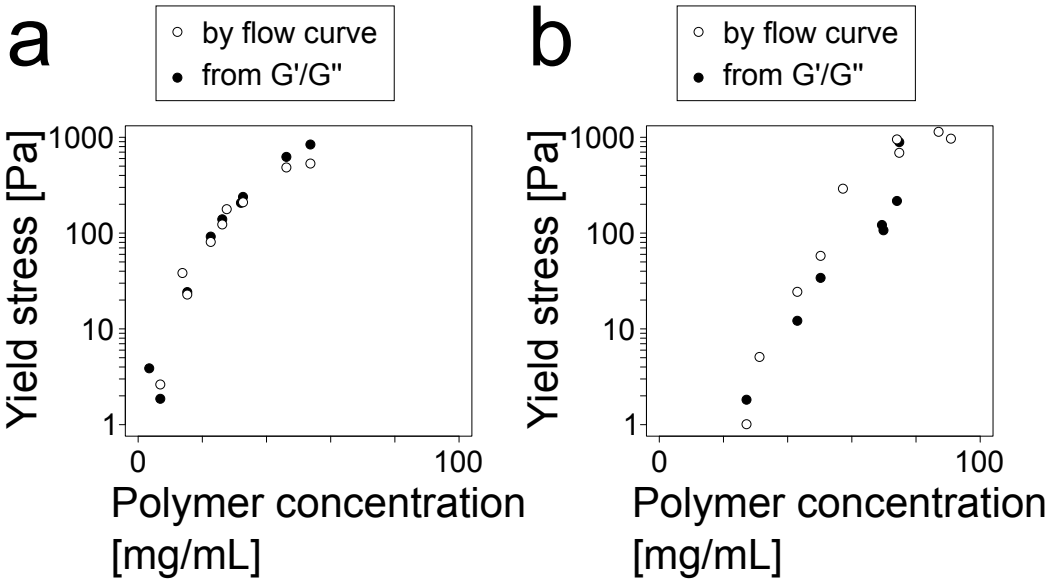

Figure C4. Yield stress as a function of polymer concentration measured from the low-strain-rate plateau in flow curves ("by flow curve") as compared to estimation using the intersection of G' and G'' curves in oscillatory shear rheology ("from G'/G''"). a) EPI scaffold. b) Sephacryl S200.

Figure C4 directly compares estimation of the yield stress from flow curves and from the intersection of G' and G'' curves for the EPI biomaterial (Figure C4a) and the Sephacryl S200 reference material (Figure C4b). There is qualitative agreement between the two measurement techniques in both cases, with a better quantitative match for the EPI biomaterial. Overall, there does not appear to be a general pattern or fundamental between the two techniques. The larger differences for the Sephacryl S200 reference material are probably due to technical difficulties: The Sephacryl S200 materials yields in a rather brittle and sudden manner, and small differences in sample arrangement might have more importance for this material than for the EPI biomaterial with its well-defined, but nevertheless relatively smooth onset of flow.

In addition to the comparison between the two methods, Figure C4 also indicates that at similar polymer concentration, the EPI biomaterial has a higher yield stress than the Sephacryl S200 reference material. This is in line with its higher stiffness, as expressed by its higher modulus at similar polymer concentration (Supporting Information associated with the main publication[1], Figure S11).

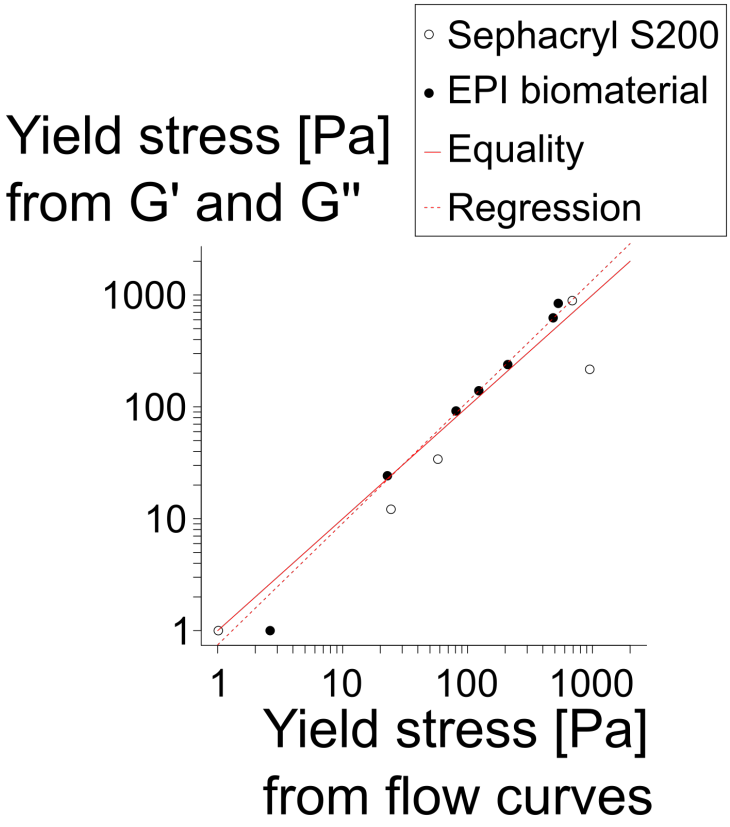

Figure C5. Comparison of yield stress evaluation from flow curves and from G'/G" crossink in oscillatory shear rheology. The solid red line denotes equality, the dashed red line Siegel[9] regression (non-parametric). Statistical details in "Statistical Reporting.xlsx", item 69.

To assess the relation between the two methods for shear stress evaluation more precisely, we evaluated the yield stress both using a shear-rate ramp in linear shear rheology and plotted the results against each other. Figure C5 shows the resulting scatter plot for the both the Sephacryl S200 reference material and the EPI biomaterial.

Linear regression analysis (using Siegel regression[9] due to non-normality of the residuals) on the logarithmic scale as shown in Figure C5, on the pooled data from the EPI biomaterial and the Sephacryl S200 reference suspension gives a slope of 1.09, which is not significantly different from 1 (Item 69, "Statistical Reporting.xlsx"). This implies good correlation between the yield stress measurements by flow curve vs. by G'-G" intersection, although it lies in the nature of statistics that more subtle differences cannot be ruled out.

4. Rheology setup details

This section describes technical details of our rheology setups.

4.1. Setups used: Cup and plate-plate in comparison

We tested several setups for rheology: a custom-made cup geometry based on the cylindrical rotor Z20 DIN 53019 / ISO 3219, Haake ref. 222-1278 (see below), plate-plate geometry (Haake PP20, ref. 222-0586), and initially also a rotary vane (FL16, Haake 222-1326).

The custom cup requires large volumes of sample, but efficiently limits evaporation and thus provides stable measurement, including for tests that take hours or days, as for instance the self-healing screens (Figure 3l and 3m in the main text[1], chapter 8 of the associated Supporting Information). However, when analysis of small samples is required for practical (ejection from 1mL syringes) or economical reasons (HA ctl, studies with many parameters and samples), the cup geometry is not suitable.

The rotary vane geometry also uses a large sample volume since a cup has to be filled (Cup DG41, Haake 222-1466). Rotary vane measurements are more stable even if after yielding, very large rotation rates are achieved, since the sample is only moved near the relatively small vane. However, the vane causes sharp gradients of shear strain and stress near the blades, such that qualitative, rather than quantitative evaluation of material characteristics (G' and G'') should be performed[8]. For this reason, we did not maintain the vane among the final setups.

The plate-plate geometry finally uses the lowest amount of sample (1mL or less for narrow gaps). The use of this setup with the EPI material is however challenging. Pore fluid is easily squeezed out by vertical movement of the chuck used to adjust the gap and it is difficult the evenly distribute the highly elastic material. These problems are specific the EPI material, since the more viscoelastic HA ctl material could be filled without problems.

Giving these overall characteristics, we preferentially use the custom cup geometry, except for if there are compelling reasons to use one of the other two geometries. Table C1 below summarizes the different geometries used.

Figure	Geometry	Comment
3f	Custom cup	
3g	Custom cup for EPI, Plate-plate for HA ctl	HA ctl: 50mL of test volume is not affordable. See comparison of plate-plate to cup measurement for EPI, Figure C6 below.
3l, 3m	Custom cup	Long experiments: Evaporation control important
5b/5c	Plate-plate, but pooled with some custom cup measurements for EPI	Many samples, cost reasons
5d-5g	Plate-plate	Many samples

Table C1. Geometries used for different rheological experiments.

4.2. Custom cup geometry

Figure C6 shows the geometrical dimensions of the custom cup geometry used.

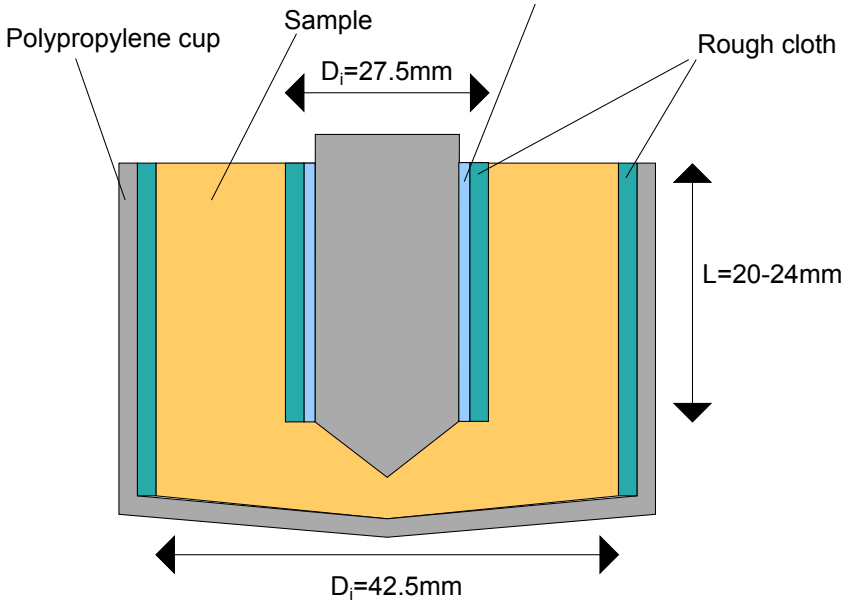

Figure C6. Cup setup for rheological measurements. A polypropylene cup (outer diameter 49mm, fitting into the cup holder for the Rheostress RS60) is lined with a rough cloth (Miobrill, Migros Switzerland, ref. 7065.206 / 15.02.2330, using hot glue). Likewise, a rough cloth is attached to the rotor (using a silicone sleeve for protection of the rotor). The setup defines a shearing cleft with an inner radius of R_i=Di/2=13.75mm, and outer radius of R_a=D_a/2=21.25mm and effective height of about 22mm, depending on the exact fill level.

From the geometrical parameters, the rheological measurement constants regarding conversion of shaft rotation to shear strain (the factor M)[8] and conversion of applied to torque to estimated shear stress (the factor A)[8]. These are:[8]

$$M = \frac{1+\delta^2}{\delta^2 - 1} = 2.44$$

and

$$A = \frac{1}{2\pi L (D_i/2)^2} = 38300 m^{-3}$$

for L=22mm. With M and A defined, we could define a custom cylinder geometry in the Rheowin software. However, both M and A should be considered approximate, because they do not include correction for forces arising on the relative large lower face[8] and also on a fundamental level, because they are derived for strain- and stress- independent materials and thus only approximately valid for more general behaviors with softening and yielding.

4.3. Plate-plate geometry

A schematic drawing of the plate-plate geometry can be found in "Statistical Reporting.xlsx", Figure S2-1A. Indeed, we used this setup also for assessment of the

rheological response of intact scaffolds, and used the fact that the scaffolds could be held in place by slight squeezing (ca. 10% deformation) between chuck and opposing plate.

This setup is predefined in the Rheowin software, and we do not need to calculate the rheometry constants A and M.

The plate-plate geometry is frequently used and convenient for small samples, especially samples containing larger particles.[8] Further, since the geometry is preconfigured in the Rheowin software, the complexity of calculating and entering the rheological constants (see above) is avoided.

It was therefore our aim to measure the rheological behavior of the EPI scaffolds also in this geometry. Loss of pore fluid is a main challenge with the EPI biomaterial. At lower concentrations (below 25mg/mL and especially below 20mg/mL), this is accentuated by increasing softness, making handling during filling without loss of fluid by capillarity or accidental squeezing more likely. At higher concentrations (above 30mg/mL at loading), contact between the plates and the sample tends to be lost more easily at yielding. There is however a window in the range of 25mg/mL to 30mg/mL available for reasonable accurate measurements.

In particular, we achieved measurement of a series of EPI biomaterial samples with a nominal polymer concentration of 28mg/mL in the plate-plate geometry. We estimate the actual polymer concentration during measurement to lie about 20% higher. First, when approaching the upper plate, we already compress the sample to some extent to ensure approximate contact;[10] we then found that we needed to apply an additional axial compression by the chuck by 10% to ensure proper measurement without slippage. We estimate that this results in a total of about 20% compression, resulting visibly in corresponding pore fluid loss. The problem is specific to the EPI scaffold samples, with HA ctl samples, the cleft between the top plate (chuck) and bottom plate could be filled smoothly.

Given the loss of pore fluid, we compared the plate-plate measurements (28mg/mL polymer concentration in EPI biomaterial, small samples from same bulk stock solution, N=8), to a cup measurement at a 20% larger concentration (33mg/mL, single 50mL sample). This provides both an approximate comparison between the two geometries and a rough estimation of sample variability at a given intended concentration from the plate-plate measurement.

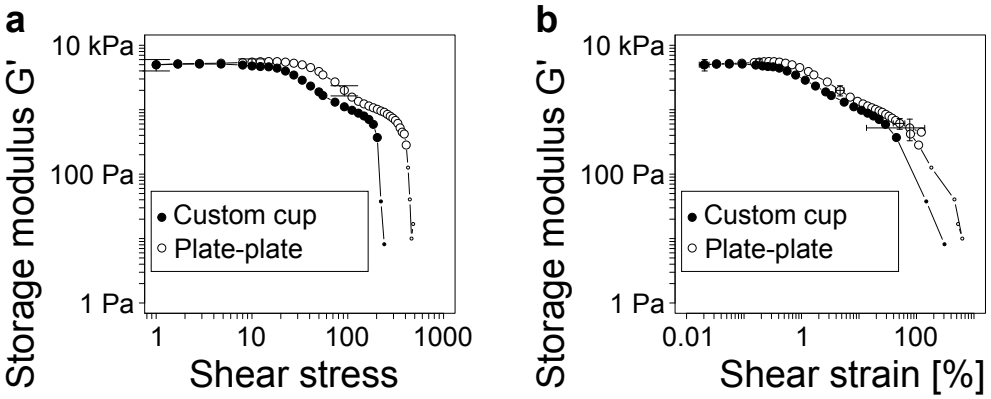

Figure C7. Comparison of measurements in the plate-plate rheometer geometry to the custom cup geometry. For the plate-plate geometry, EPI biomaterial at 28mg/mL concentration was loaded between the plates, applying a supplemental 10% compression after gently squeezing the samples between upper and lower plate. For the custom cup geometry, EPI biomaterial was prepared at 33mg/mL to match the anticipated increase in concentration in the plate-plate geometry during compression. A) Storage modulus as function of applied stress. B) Data replotted as a function of estimated shear deformation. Error bars are equal to one standard deviation for the plate-plate measurements (N=8) and for clarity are only indicated on illustrative points; the cup measurement is a single measurement.

Figure C7 shows the results. The softening transition is clearly visible in both measurement configurations. This rules out the (unlikely) hypothesis that the softening transition would be an artifact arising from a particular interaction of the cup geometry with the EPI material. Indeed, the softening transition cannot arise from our custom cup geometry alone as we found no detectable double transition for the Sephacryl S200 material in Figure 3h in the main text. Despite this, the demonstration of the elastic softening transition with a second geometry as compared to the custom cup data used mainly is important, as it points towards a general, rather the setup-linked behavior.

Further, the G_0' value measured at low strain is similar between the cup and the plate-plate geometry when taking into account sample concentration by compression.

The difference between the two geometries, from what can be said given the limited data available, seems to arise at higher stresses. This is probably linked to the more inhomogeneous shear stress distribution in the plate-plate geometry as compared to the relatively narrow cleft in the cup geometry.[8] For example, the yield strain, by linear interpolation in the logarithmic scale shown in Figure C7b, is estimated to 57% for the cup geometry, but to 152% +/- 5% for the plate-plate geometry (for the samples compared). There is probably some bias towards higher yield strain in the plate-plate geometry, most likely linked to the need to apply about 10% uniaxial compression to ensure tight contact between the plates and the materials. It is however certainly lower than the data here seems to suggest, since the 57% yield strain obtained for the particular sample used here is one of the lowest yield strains observed for all EPI samples (see Figure 5b in the main text[1]). Summing up, while our data suggests qualitatively similar behavior of the EPI biomaterial in both cup and plate-plate geometry, there are reasons to believe that the high stress features are biased towards too high values. Regarding this, and also to reduce the influence of evaporation in longer experiments, we prefer in principle the custom cup geometry in general, if compatible with sufficient sample provision.

5. Self-healing assessed under oscillatory shear rheological testing

This section provides additional data and analysis for the self-healing experiments shown in Figures 3l and 3m in the main script as well as chapter 8 of the Supporting Information associated with the main publication[1]. This concerns a graphical display of

the complete data (Figure C8), analysis of robustness parameters (repeatability between runs and samples)

5.1. Complete self-healing data-set

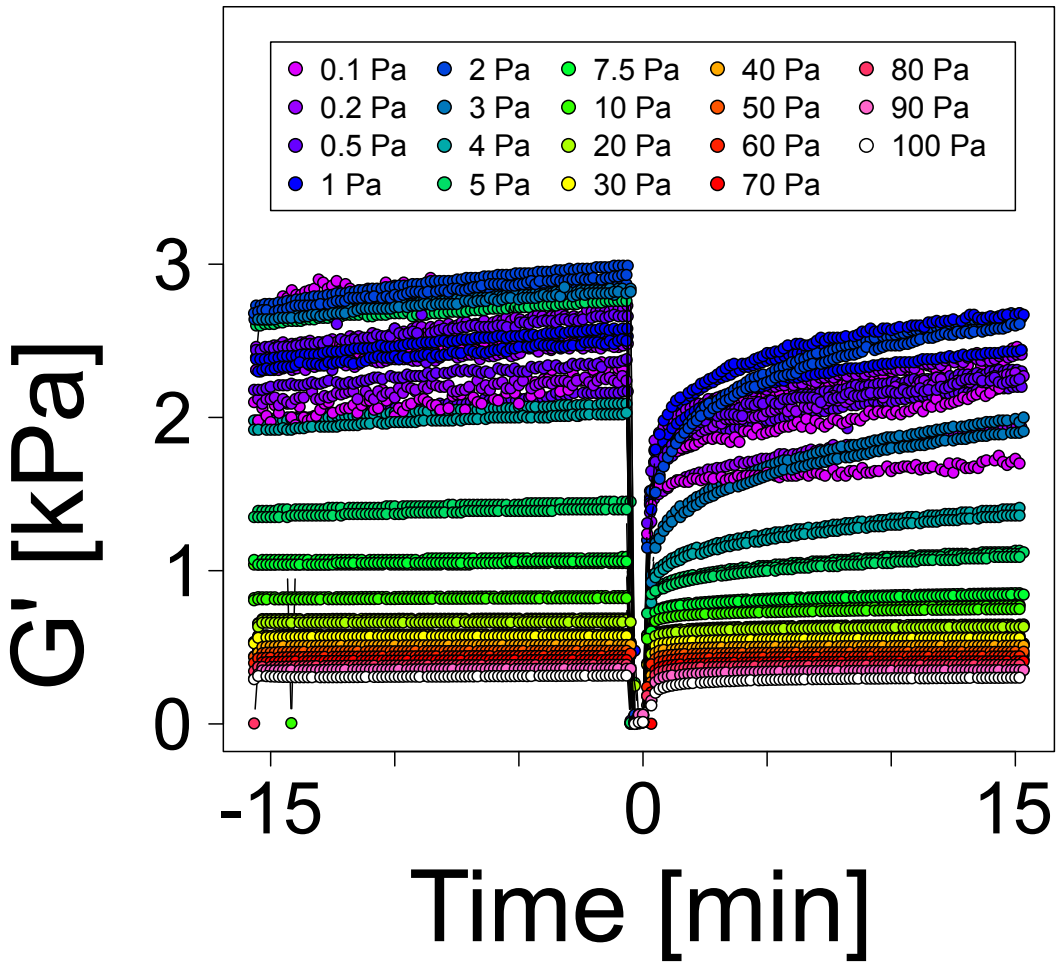

Figure C8: Self-healing of the EPI biomaterial probed by under continuous oscillatory shear rheology at 0.2Hz and predefined shear stress level, complete dataset. For each of the predefined shear levels (0.1Pa to 100Pa, see legend), 2-3 experimental runs were carried out. Each experimental runs consists in an baseline equilibration period with constant application of the predefined oscillatory shear level (theoretically from -15min to -30s), followed by 30s of strong oscillatory shear to emulate injection (200Pa), followed by recovery period (theoretically, 0min to 15min) with again constant application of the predefined shear level. Nominally, a G' (and G'') value are evaluated every 10s (2 shear cycles).

Figure C8 gives an overview of the full dataset about self-healing of the EPI biomaterial under predefined oscillatory shear loads.[10] We predefined continuous oscillatory shear stress levels to be applied (from 0.1Pa to 100Pa, see Figure C8). For each of the 19 shear stress levels shown in Figure C8, we carried out 2 to 3 self-healing experiments (we used two distinct samples from a single stock solution with a polymer concentration of

23.8mg/mL; we carried out two consecutive self-healing experiments on one of the two samples). Each such experiment consists in a 15min pre-equilibration period where the chosen shear stress level is applied in oscillatory mode at 0.2Hz. It is then followed by a brief strong shear period to emulate liquefaction during ejection (200Pa, 30s).[10] Recovery of the mechanical properties by self-healing is then followed during a 15min recovery period, by continuous application of the same shear level as the one used for the equilibration period. During the entire experiment, G' (and G'', not shown) values are evaluated every 10s (after completion of 2 cycles of oscillatory shear). Given the long duration of the entire sequence, we used a solvent trap to avoid evaporation and ran the experiments consecutively from a pre-programmed Rheowin job.

5.2. Normalization and averaging

Averaging over the different samples and runs per probe yield stress is presented and discussed for Figure S16 in the Supporting Information of the associated publication[1].

5.3. Repeatability

5.3.1. Successive repeatability

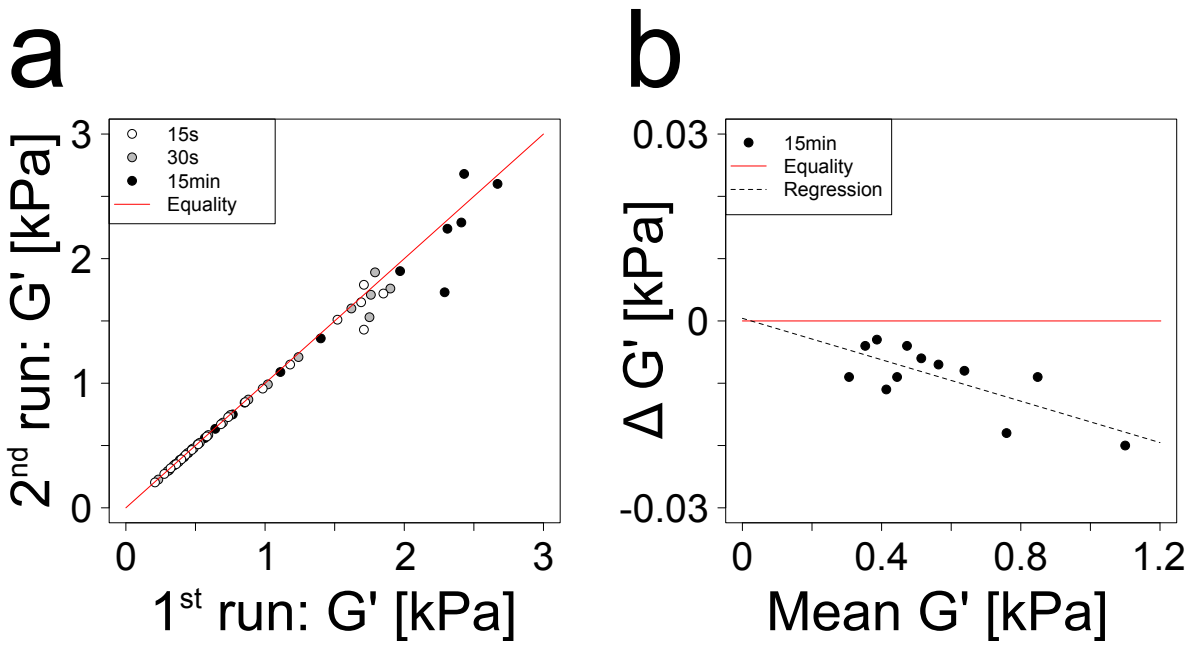

Figure C9: Correlation between 1st and 2nd self-healing experiment on a single sample. a) G' values recovered at 15s, 30s, and 15min, for various continuously applied shear stress levels. Values obtained in the 2nd are plotted against the corresponding values obtained in the 1st run. b) Bland-Altman diagram.[11] From the data in Figure C9b, the mean and the difference for each pair of associated G' values are calculated. As linear regression with statistical inference cannot be carried out on the entire dataset due to the great difference in variability, we restricted the analysis to the lower part (G' at baseline < 1.5kPa); also, to avoid inflation of statistics by correlations between timepoints, only the 15min time-point was used. The differences in G' recovered after 15min in the second vs. the first run are then plotted against the G' recovered on average. Theoretical equality lines are given for both Figure C9a and C9b with red lines. Statistical details in "Statistical Reporting.xlsx", item 39.

For one of the two samples examined, we carried out two consecutive self-healing scans. This allows us to detect potential material fatigue, which would lead to lower mechanical strength during the second self-healing scan, and thus to exclude that we merely observe progressive material destruction by the extended shearing and thus progressively lower mechanical properties.

Figure C9 compares the recovery of G' obtained in the first self-healing run to the recovery of G' in the second run. In Figure C9a, the G' values recovered at 15s, 30s and 15minutes, under various levels of constantly applied shear stress, are plotted against each other for the two runs. We attempted linear regression, but due to the very unequal variance, normality of the residuals cannot be achieved even with the use of generalized linear models. The origin of the great disparity in variance between low G' points and high G' points in Figure C9a is unclear. On the one hand, high G' points are associated with low probing stress, approaching the technical limits of force and displacement detection by the Rheostress 100 machine. This would contribute technical noise to these measurements. On the other hand, we have also observed that self-healing not only takes time, but is favored by slight mechanical movements (peak of recovered G' at probing shear stress values around 1Pa rather than at the lowest applied values in Figure 3k). It is difficult to reconcile continuous monitoring of self-healing at a given probing shear stress with preconditioning procedures which would be optimal at some generally different shear stress, and thus, the high variability at the lowest probing stress (highest G' values) may also have methodological roots.

Nevertheless, to better quantify possible loss of mechanical strength due to the numerous shear periods, we resorted to Bland-Altman plots, designed to reveal differences between associated measurements.[11] To reduce heteroscedasticity, and enable statistical inference from linear regression, we restricted the data to the points with a baseline G' value below 1.5kPa., Figure C9b shows a Bland-Altman[11] plot (difference between associated values plotted against their mean value). To avoid inflation of test statistics by inappropriately correlated data values, we restricted the analysis to the 15min recovery time-point.

Linear regression in a Bland-Altman[11] plot is focused on the differences, rather than the similarities between the two measurements, and interpretation of the results needs to be carried out in this context. We obtain an intercept of -0.0004kPa (95% confidence interval from -0.006 to +0.007 kPa), statistically non-significant (P=0.11). This implies that to within very high precision, there is no detectable additive bias between the second and first measurement on the same sample.
Regarding the slope, we obtain an estimate of -0.017 (95% confidence interval from -0.027 to -0.006). This corresponds to a proportional loss of mechanical strength of 1.7%. For all practical purposes in biomaterial, this indicates reliable conservation of mechanical properties throughout the shearing periods. However, due to the exceedingly low variability in the restricted dataset, this result is still statistically significant ($P=6.2*10^{-3}$, "Statistical Reporting.xlsx", item 39). This indicates that there is practically negligible, but technically detectable, overall decrease in material strength from the 1st to the 2nd self-healing experiment.

Due to the restricted dataset used for regression, caution needs to be applied: There is a slight, but detectable decrease of mechanical strength when monitoring at sufficiently high monitoring stress (here, this threshold is 5Pa). This difference is also detectable on the entire dataset by a non-parametric test (Paired Wilcoxon ranking test, $P=2*10^{-3}$, "Statistical Reporting.xlsx", item 39), but as outlined above, linear regression on the whole dataset is invalid due to excess heteroscedasticity.

Given the relative change in the percent range after nearly 20 liquefaction periods, and the intended use as an injectable with a single liquefaction step, the material is clearly sufficiently robust for its intended application. It is further unclear whether this minimal material fatigue results from internal friction and particle damage, or whether it is related to interaction with the rough surfaces in the rheometer.

5.4. Sample to sample variation

We also analyzed sample-to-sample variation by running a self-healing experiment on two distinct samples, from the same stock solution to ensure identical polymer concentration. We again find strong correlation between the G' values obtained at similar time points (Figure C10a), with a steep change in variability. For reasons similar to the previous intra-sample analysis, we restrict Bland-Altman analysis[11] to data points with less than 1.5kPa baseline G', and to the 15min time-point. The resulting Bland-Altman diagram is shown as Figure C10b. We find no significant correlation by linear regression, and also not by non-parametric Wilcoxon testing without the 1.5kPa restriction. This implies that on the two samples examined, we find no significant difference in self-healing behavior.

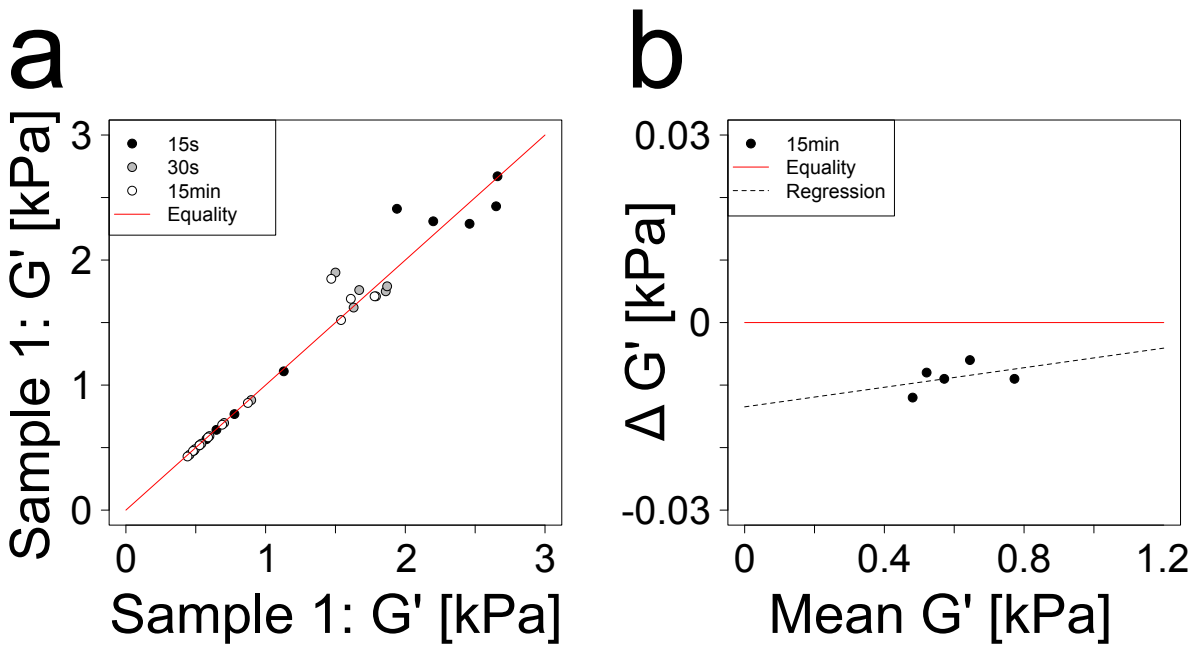

Figure C10: Correlation between the self-healing results on two samples of biomaterial. a) G' values recovered at 15s, 30s, and 15min, for various continuously applied shear stress levels. Values obtained for sample 2 are plotted against the corresponding values obtained for sample 1. b) Bland-Altman diagram[11]. From the data in Figure C10a, plot of differences

against the mean for each associated pair of G' values. Restriction to values with an initial G' value below 1.5kPa for normality of the residues, and to the 15min time-point to avoid test statistic inflation by correlated values. Theoretical equality lines are in red. Statistical details in "Statistical Reporting.xlsx", item 40.

6. Time course and probing stress

Figure 3l and Figure 3m in the main text[1] suggest that not only the final extent, but also the time-course of self-healing depends on the applied level of probing stress. There is a very rapid initial recovery (time-scale of seconds), followed by slower recovery of baseline G'; the slow recovery is quantitatively more important at lower probing stress, but there seems to be a peak with the highest, and also somewhat more rapid recovery near 2Pa of probing stress.

Here, we better quantify the slower part of the stress recovery. We do by evaluation of the relative increase of G' from the 30s measurement time-point to the 15min recovery time point. The higher the relative increase during this phase, the higher and possible more efficient the contribution of the slow recovery.

Figure C11 shows the results for selected, logarithmically spaced probing stresses. The analysis confirms the visual impression from Figure 3l and 3m in the main text[1]: Generally, slow recovery is quantitatively more important at low probing stress than at high probing stress, but there is a peak around 2Pa where it is most important (P=0.012, t-test comparing relative increase in G' for 0.2Pa and 2Pa, item 41 in "Statistical Reporting.xlsx"). On the soft plateau at high probing stress (20 and 50Pa in Figure C11), smaller values of G' are recovered (Figure 3l in the main text[1]), but the G' recovery occurs more rapidly. Indeed, for 20 and 50Pa probing stress, the relative G' increase is less than 10%, compared to about 30% at very low stress (P=0.011, 0.2Pa vs. 50Pa probing stress, item 41 in "Statistical Reporting.xlsx").

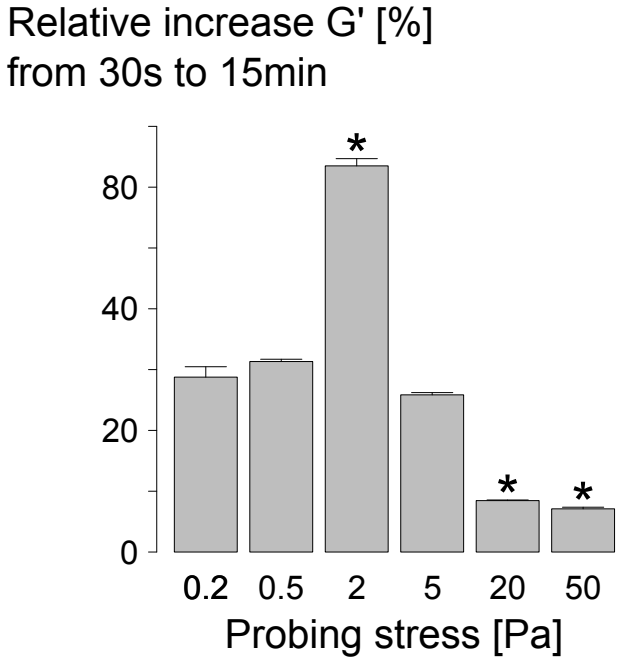

Figure C11: Increase in G' from 30s self-healing to 15min self-healing. The plot indicates relative increase in G' (in percent) obtained as the ratio of G' at 15min to the ratio of G' at 30s minus 1 time 100%. Testing of each condition against the 0.2Pa probing stress. Testing details in item 41, "Statistical Reporting.xlsx".

7. Nonlinear contact law for quantitative simulation

We designed the EPI meta-biomaterial on the basis of qualitative numerical simulation (Figure 2 of the associated publication[1]). The main aim there was simplicity to gain a basic understand of the requirements for EPI meta-biomaterial design.

However, to be of more direct practical use, we find it important to provide a closer quantitative model as well. Particularly, for Figure 5e of the main text[1], the aim was to precisely identify the effect of collagen coating on the microscopic properties of the EPI biomaterial particles. This information is not easily accessible from macroscopic observation or rheological measurements, but it can be estimated by comparing observed changes to simulated known parameter changes.

To enable this approach, a reasonably precise agreement between the observed rheological properties of the EPI biomaterial and a baseline simulation needs to be established. We therefore set out to match not only qualitatively, but quantitatively the rheological shear modulus G' in large-scale strain sweeps.

Once quantitative matching between empirical and simulated rheological oscillatory sweeps achieved, the effect of collagen coating can then be modeled by changing plausible individual parameters of the simulation.

7.1. Porosity and force contact law

In the numerical simulations, the force arising from compressive contact between neighboring elements needs to be specified as a function of the relative compression occurring. The relation between relative compression (compressive strain) and the resulting force (or, if quantified per area, stress) is referred to as the "contact law". Various models for this contact law exist; details of the implementation of the contact law in the base simulation, with central reinforcement to avoid particle interpenetration, can be found in the Python particleShear manual (located at /code/Documentation/ Simulation particleShear/Manual particleShear.pdf, part I). Here, specific additions to emulate highly compressible are described. Approximately, contact laws can be obtained empirically by uniaxial compression of bulk material.

Figure C12 shows the measured contact laws, along with relevant theoretical models. The empirical estimation of the contact law was obtained by monitoring of the force during uniaxial compression testing of bulk samples (disk geometry). The compressive strain is the calculated from the relative change of sample height compared to the original, free height, while the compressive stress is the force par unit of sample area.

Measurements were conducted on submerged samples to minimize contribution of hydrostatic and capillary forces.

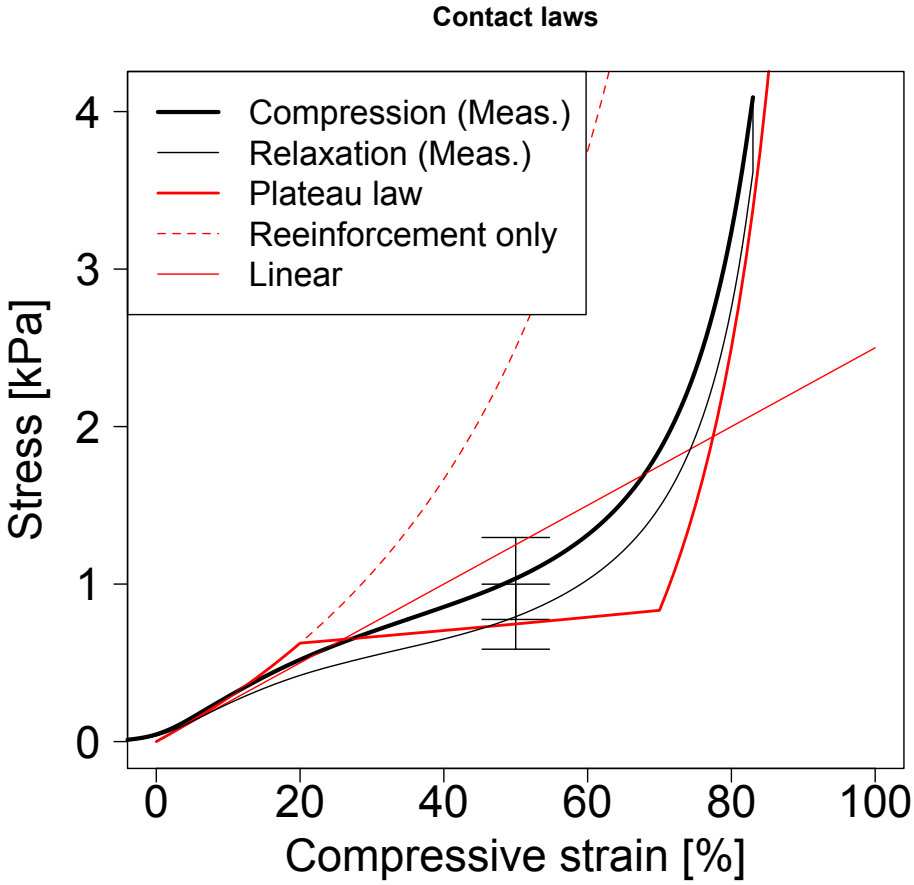

Figure C12. Contact law, empirical estimation by uniaxial compression of bulk material along with various theoretical models. N=7 for the empirical evaluation, compression and relaxation rate 0.01mm/s, sample diameter 19-22mm, sample height 6-10mm. The linear contact law is the basis for the simulations by Otsuki et al.[12], while for the primary simulations in Figure 2 of the main text[1], we used a central reinforcement ("Reeinforcement only" in Figure C12, to avoid entangling of neighboring networks (see manual at / code/Documentation/ Simulation particleShear/Manual particleShear.pdf, part I, section 4.4). The plateau law, explored in this document and Figure 5e in the main text[1], affords a more realistic description of the rheology of the EPI meta-biomaterial.

In Figure C12, three distinct regions can be noticed for the empirical compression law: an initial strong rise, followed by an inclined plateau, giving finally rise to a steeply rising force curve. This is true both in compression and subsequent relaxation. This behavior is well known for highly porous, foam-like substances: the initial rise is the elastic region, the plateau arises through buckling mechanisms, while the final rise corresponds to densification with progressive loss of free pore space.[13]

Figure C12 also shows three different theoretical contact law models in comparison. All three were calculated with a low-strain elastic modulus (slope) of 2.5kPa to obtain an order-of-magnitude fit with the empirical curves. The simplest model is the linear model; this was used by Otsuki et al.[12] in their simulation of frictional spherical microgel suspensions. While successful at low strain,[12] this approach proved problematic at higher shear deformation, since linear force implies that it is possible to merge

neighboring elements completely with finite force. This is unphysical and leads to problems with entanglement between neighboring networks. Due to our aim of developing large yield-strain materials, we were particularly interested in the large strain response and so found a simple linear response to unsuitable for our purposes. For this reason, for the simulations shown in Figure 2 in the main text[1], we used a non-linear contact law that follows the linear law at small deformations but diverges when the distance between neighboring sphere elements approaches zero ("Reeinforcement only" in Figure C12). This type of contact law enabled the desired simulation at large-scale deformation presented in Figure 2 in the main text[1]. As one can see from Figure C12, this comes at the cost of deviation from the actual, observed contact law.

Since the plateau in the force contact law results from large porosity fractions[13], using the "Reeinforcement only" contact law can be anticipated to work to some extent against the effects of porosity. For this reason, we implemented the possibility of arbitrary contact laws in our simulation framework, and in particular also provided the possibility to superimpose a step-wise varying relative slope with the non-linear contact law. Such a hybrid contact law is shown in Figure C12, labeled "Plateau law". At this stage, one can anticipate that it should be possible to better capture the multiphasic behavior of highly porous materials with that type of contact law, although it is still difficult to capture exactly all aspects including steeply rising densification.

7.2. Comparison of simulation and rheological master curve

We next proceeded with direct confrontation of simulation and measured rheological master curves. There are clearly a number of important limitations to this direct comparison: the simulations are 2D, the material is 3D; also, in the simulation, the porosity is simulated in part by removal of crosslinks, and in part emulated by the plateau contact law while in reality, the hydrogel wall material would in all likelihood not exhibit a plateau contact law, this being a unique feature arising through the porosity and foam-like structure.[13]

Nevertheless, for the purpose of better understanding the rheological behavior of the EPI meta-biomaterial, as well as to gain an insight into how various model parameters would affect the actual rheological properties of the EPI meta-biomaterial, we found it useful to attempt to tune the simulation in such a way as to more quantitatively match the empirical rheological curves.

Figure C13 shows the rheological master curve (stress and G' values normalized to low-strain G') of the EPI meta-biomaterial in comparison with the original simulation ("Simulation: Simple") as well as with an adapted simulation using a plateau contact law ("Simulation: High porosity"). The parts of the curves that correspond to a solid-like behavior (G'>=G'') are shown in thick lines respectively large symbols. The error bars and dashed lines represent one standard deviation.

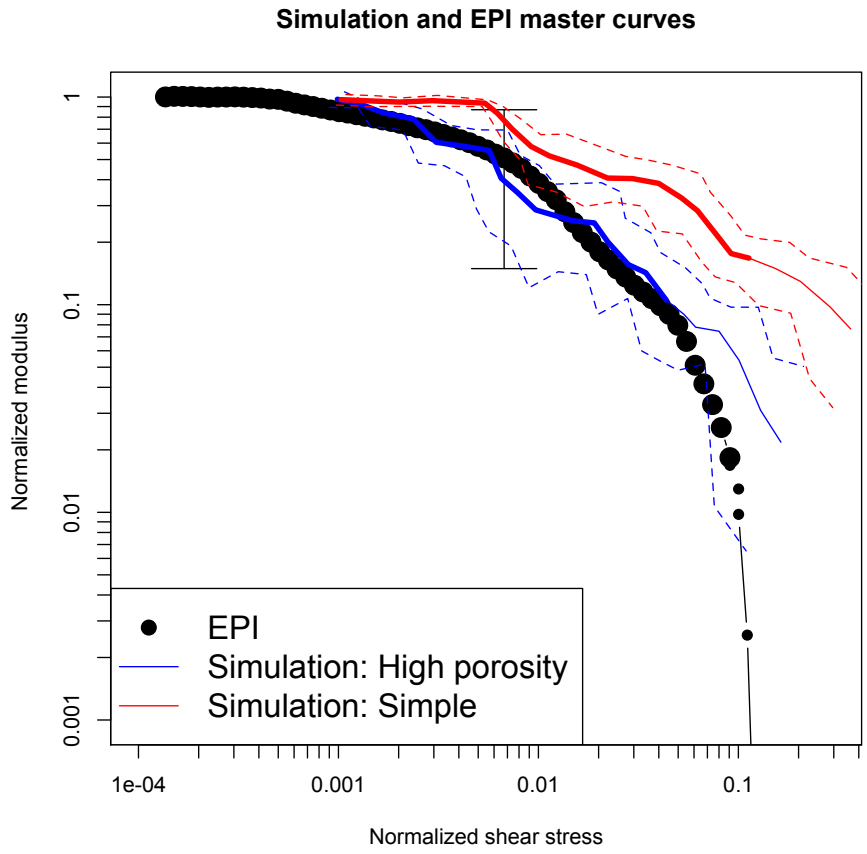

Figure C13. Rheological master curve, measured on EPI-biomaterial in comparison with the "simple" simulation (diverging contact law, as used for Figure 2 in the main text[1]), and in comparison with"high porosity" simulations using a plateau contact law as shown in Figure C12. Thick colored main lines respectively large symbols indicate the regions with solid-like behavior (G'>=G''), while thin colored lines respectively small symbols indicate liquid-like behavior (G''>G'). The dashed lines correspond to one standard deviation. Statistical details in Supplementary 11, item 76.

From Figure C13, it can be seen that while the simple simulations used for Figure 2 correctly predict the occurrence of elastic softening (lowering of the relative modulus to values substantially below 1 well before liquefaction), they quite dramatically underestimate the magnitude of the elastic strain softening effect. Using a more sophisticated plateau-contact law much better emulates the effect of strong porosity by providing near quantitative matching of the actual observed rheology of the EPI meta-biomaterial. For example, at a relative yield stress of 0.05, the difference between the observed rheological response and the simulated relative modulus is highly significant for the simple diverging contact law ($P=3.6*10^{-6}$, Wilcoxon test with Bonferroni correction for two tests, "Statistical Reporting.xlsx", item 76), while using the plateau law abolishes most of the difference (P=0.057, "Statistical Reporting.xlsx", item 76).

Hence, the results presented here further highlight the extreme importance of porosity for the elastic softening transition. They also provide a basis for quantitative modeling of the EPI meta-biomaterial.

8. Bibliography

1 Beduer, A. *et al.* An Injectable Meta-biomaterial: From Design and Simulation to In-vivo Shaping and Tissue induction. *Adv Mater* **DOI: 10.1002/adma.202102350** (2021).

2 Evans, I. D. & Lips, A. Concentration-Dependence of the Linear Elastic Behavior of Model Microgel Dispersions. *J Chem Soc Faraday T* **86**, 3413-3417, doi:DOI 10.1039/ft9908603413 (1990).

3 Popov, L. V. *Contact Mechanics and Friction*. (2017).

4 xlib_.jar (ftp://ftp.empa.ch/pub/empa/outgoing/BeatsRamsch/lib/, 2015).

5 Münch, B. & Holzer, L. Contradicting Geometrical Concepts in Pore Size Analysis Attained with Electron Microscopy and Mercury Intrusion. *Journal of the American Ceramic Society* **91**, 4059-4067, doi:10.1111/j.1551-2916.2008.02736.x (2008).

6 Schindelin, J. *et al.* Fiji: an open-source platform for biological-image analysis. *Nat Methods* **9**, 676-682, doi:10.1038/nmeth.2019 (2012).

7 Bhattacharjee, T. *et al.* Polyelectrolyte scaling laws for microgel yielding near jamming. *Soft Matter* **14**, 1559-1570, doi:10.1039/c7sm01518f (2018).

8 Schramm, G. *A Practical Approach to Rheology and Rheometry*. (Gebrueder HAAKE GmbH, 1994).

9 Siegel, A. F. Robust Regression Using Repeated Medians. *Biometrika* **69**, 242-244, doi:10.2307/2335877 (1982).

10 Chen, M. H. *et al.* Methods To Assess Shear-Thinning Hydrogels for Application As Injectable Biomaterials. *Acs Biomater Sci Eng* **3**, 3146-3160, doi:10.1021/acsbiomaterials.7b00734 (2017).

11 Bland, J. M. & Altman, D. G. Statistical methods for assessing agreement between two methods of clinical measurement. *Lancet* **1**, 307-310 (1986).

12 Otsuki, M. & Hayakawa, H. Discontinuous change of shear modulus for frictional jammed granular materials. *Phys Rev E* **95**, 062902, doi:10.1103/PhysRevE.95.062902 (2017).

13 Gibson, L. J. & Ashby, M. F. *Cellular Solids: Structure and properties*. (Cambridge University Press, 1997).